Earth Planet. Sci. Lett. 674 (2026) 119759

Contents lists available at ScienceDirect

Earth and Planetary Science Letters

journal homepage: www.elsevier.com/locate/epsl

Orographic and convective precipitation control meteoric ^{10}Be wet depositional fluxes at low latitude

Rose PAQUE [a], Angus MOORE [a], Jean L. DIXON [b], Marcus CHRISTL [c], Yessenia MONTES [d], Veerle VANACKER [a,e,*]

[a] Earth and Life Institute, Center for Earth and Climate Research, UCLouvain, Louvain-la-Neuve, Belgium
[b] Department of Earth Sciences, Montana State University, Bozeman, USA
[c] Laboratory of Ion Beam Physics, ETH-Zurich, Switzerland
[d] Facultad de Ingeniería en Geología, Minas, Petróleo y Ambiental (FIGEMPA), Universidad Central del Ecuador, Quito, Ecuador
[e] Soil Geography and Landscape Group, Environmental Sciences, Wageningen University & Research, Wageningen, The Netherlands

ARTICLE INFO

Editor: Dr Y Asmerom

Keywords:
Meteoric ^{10}Be
Wet deposition
Orographic precipitation
Convective precipitation
Depositional fluxes

ABSTRACT

Using meteoric ^{10}Be (^{10}Be$_m$) as a tracer of Earth surface processes requires understanding the factors that control ^{10}Be$_m$ depositional fluxes. How precipitation influences ^{10}Be$_m$ depositional fluxes is still debated, especially at low latitudes where little empirical flux data exist. To investigate how precipitation amount and type (drizzle vs. intense rain) influence meteoric ^{10}Be depositional patterns in equatorial regions, we measured ^{10}Be$_m$ concentrations in rain across a 10-fold precipitation gradient on Santa Cruz Island in the Galápagos Archipelago (Ecuador) over one hydrological year. The island's climate is characterized by a cool season, with aridity in the lowlands and persistent fog and drizzle in the highlands, and a warm season marked by localized, intense convective precipitation. Measured ^{10}Be$_m$ concentrations during the warm season decrease with increasing precipitation. Conversely, during the cool season ^{10}Be$_m$ concentrations increase with increasing precipitation. We attribute this behavior to dilution of ^{10}Be$_m$ concentrations during intense precipitation events in the warm season and enhanced efficiency of scavenging of ^{10}Be$_m$ bearing aerosols by fog droplets during the cool season. Overall, enhanced scavenging outweighs dilution, and annual fluxes show a greater-than-linear increase with precipitation. Our dataset demonstrates that ^{10}Be$_m$ concentrations in rain near the equator vary spatially and temporally as a function of precipitation type. We recommend taking atmospheric processes leading to cloud and fog formation into account when assessing wet depositional fluxes of ^{10}Be$_m$, as these may enhance ^{10}Be$_m$ scavenging from the atmosphere.

1. Introduction

Meteoric beryllium-10 (^{10}Be$_m$) is a valuable tracer for investigating land surface processes over temporal scales ranging from 10^3 to 10^6 years (Willenbring and von Blanckenburg, 2010). Numerous studies have used ^{10}Be$_m$ to assess soil ages and residence time (Bacon et al., 2012; Egli et al., 2010; Pavich et al., 1985), date sedimentary archives (Lebatard et al., 2010), and quantify soil erosion rates at the hillslope (Jungers et al., 2009; Monaghan et al., 1992; Schoonejans et al., 2017; West et al., 2013) and catchment scales (Brown et al., 1988; Portenga et al., 2019; Wittmann et al., 2015). Production of ^{10}Be$_m$ in the atmosphere occurs through spallation reactions between cosmic rays and atmospheric N and O atoms. Production rates are highest in the stratosphere where approximately 65 % of total atmospheric ^{10}Be$_m$ production occurs and decrease with atmospheric depth so that only 35 % is produced in the troposphere (Lal and Peters, 1967; Masarik and Beer, 2009). After formation, ^{10}Be$_m$ attaches to aerosols and is deposited on the Earth's surface through wet and dry deposition. To effectively use ^{10}Be$_m$ for quantifying Earth surface processes, a comprehensive understanding of the mechanisms governing ^{10}Be$_m$ deposition rates is essential.

The flux of ^{10}Be$_m$ to the Earth's surface is influenced by several factors that control ^{10}Be$_m$ production, transport from the stratosphere to the troposphere and intertropospheric mixing, and delivery to the surface of the Earth (Lal and Peters, 1967). For example, solar activity affects ^{10}Be$_m$ production by modulating the flux of galactic cosmic rays

* Corresponding author.
E-mail address: veerle.vanacker@uclouvain.be (V. VANACKER).

https://doi.org/10.1016/j.epsl.2025.119759
Received 27 November 2024; Received in revised form 17 November 2025; Accepted 21 November 2025
Available online 3 December 2025
0012-821X/© 2025 Elsevier B.V. All rights are reserved, including those for text and data mining, AI training, and similar technologies.

reaching Earth. Solar modulation fluctuates with the 11-year sunspot cycle, as well as longer-term secular changes in solar intensity, and drives much of the variation in global average $^{10}Be_m$ production in the atmosphere over annual to centennial timescales (Beer et al., 1990; Masarik and Beer, 2009; Steinhilber et al., 2012). The Earth's magnetic field is another important factor controlling $^{10}Be_m$ production rates because the field deflects the lower-energy portion of the cosmic ray flux. Deflection is strongest at the equator and weakest at the poles. As a result, $^{10}Be_m$ production rates in the atmosphere are highest at high latitude and lowest at low latitude (Graly et al., 2011; Heikkilä et al., 2013; Masarik and Beer, 2009). Stratosphere-troposphere exchange dynamics and atmospheric circulation patterns also affect $^{10}Be_m$ distribution. The rate at which $^{10}Be_m$ is transferred from the stratosphere to the troposphere is governed by atmospheric mixing, with more vigorous stratosphere-troposphere exchange increasing the flux of $^{10}Be_m$ to the Earth's surface (Heikkilä et al., 2013). Conversely, intense convective activity at equatorial latitudes, under the rising limb of the Hadley cell, may dilute $^{10}Be_m$ concentrations in rain-forming regions of the atmosphere with ^{10}Be-poor air from low altitude (McHargue and Damon, 1991; Willenbring and von Blanckenburg et al., 2010). General circulation models (e.g. Heikkilä et al., 2009; Field et al., 2006) are informative to predict spatial patterns of $^{10}Be_m$ deposition, although the uncertainty on the model-based $^{10}Be_m$ flux remains high for the equatorial region (Willenbring and von Blanckenburg, 2010).

Direct measurements of $^{10}Be_m$ in precipitation have been instructive in determining the effects of latitude (Graly et al., 2011), stratosphere-troposphere exchange (Graham et al., 2003), altitude (Heikkilä et al., 2008), and precipitation rates (Deng et al., 2020) on short-term fluxes of $^{10}Be_m$. Yet, how precipitation influences $^{10}Be_m$ depositional fluxes on the Earth's surface remains ambiguous. Although many studies have identified a positive linear correlation between $^{10}Be_m$ fluxes and precipitation rates (e.g., Dixon et al., 2018; Graly et al., 2011), others have suggested that $^{10}Be_m$ fluxes are independent of precipitation (e.g., Heikkilä et al., 2008). A positive relationship between $^{10}Be_m$ fluxes and precipitation is described as the "additive effect" and implies that $^{10}Be_m$ concentrations in rainwater are largely independent of the precipitation rate (e.g., Brown et al., 1989). Willenbring and von Blanckenburg (2010) put forward that the additive effect is commonly observed in low-elevation sites within continental settings where most of the precipitation falls during advective events. In such settings, the empirical equation developed by Graly et al. (2011) can provide a first-order estimate of the primary meteoric ^{10}Be depositional flux (as shown in e.g. Krone et al., 2024). In island, coastal, or high-elevation sites, however, $^{10}Be_m$ concentrations tend to decrease with increasing precipitation rate, resulting in $^{10}Be_m$ fluxes that are independent of precipitation. This phenomenon is described as the "dilution effect". Heikkilä et al. (2008), for example, observed systematic differences in $^{10}Be_m$ concentrations between two high-elevation sites in Switzerland, whereby the precipitation at the highest site (with highest precipitation) had the lowest $^{10}Be_m$ concentrations. However, the study also revealed that monthly $^{10}Be_m$ concentrations can vary strongly for a given site. Willenbring and von Blanckenburg (2010) interpreted the dilution as a side-effect of convective events, where $^{10}Be_m$ is supplied at a constant rate to proximal air masses by stratosphere-troposphere exchange. Based on a re-analysis of precipitation ^{10}Be data, Deng et al. (2020) proposed that ^{10}Be flux records are subject to both additive and dilution effects, with dilution effects being more important when the atmospheric moisture is derived from local sources.

However, the above-mentioned global assessments include few data from low latitudes where atmospheric processes can be highly variable in time and space. In pioneering work at Mauna Loa in Hawaii (~20°N), Brown et al. (1989) already showed large variations in $^{10}Be_m$ concentrations between precipitation events, with occasional high-concentration events that heavily influenced overall deposition. As these variations could not be attributed to contamination, Brown et al. (1989) called for further research on the factors that control the spatiotemporal distribution of $^{10}Be_m$.

To address this knowledge gap, we studied $^{10}Be_m$ wet deposition patterns at an equatorial site in the Galápagos Archipelago and analyzed how atmospheric and climatic dynamics influence the meteoric ^{10}Be depositional fluxes. We set up five monitoring stations on Santa Cruz Island that were sampled biweekly during one hydrological year. We combined the individual rainwater collections into four representative samples to study the seasonal effect on $^{10}Be_m$ concentrations, and derived annual $^{10}Be_m$ fluxes from the measured $^{10}Be_m$ concentrations and precipitation data. Because of the unique climatic conditions of the Galápagos, the sites span a 10-fold range in annual precipitation (250 – 2500 mm), and furthermore allow us to characterize $^{10}Be_m$ wet deposition as a function of precipitation type (convective vs. orographic) (Fig. 1).

2. Study area

The Galápagos Islands are hot-spot volcanic islands in the Pacific Ocean located approximately 1000 km west of the Ecuadorian coast. The archipelago's climate is influenced by the interplay between ocean currents and the movement of the Intertropical Convergence Zone (ITCZ) (Pryet et al., 2012; Trueman and D'Ozouville, 2010). The ITCZ is a region several hundred kilometers wide from north to south where the trade winds from the northern and southern hemispheres meet. This convergence facilitates the updraft of warm, moist air, which leads to significant convective activity, characterized by frequent thunderstorms and heavy rainfall (Trueman and D'Ozouville, 2010). The ITCZ's oscillation around the equator greatly influences the intensity and frequency of convection over the Galápagos, with peak precipitation occurring when the ITCZ is positioned directly overhead (Wang and Fiedler, 2006). The atmospheric dynamics in the Galápagos are also influenced by the convergence of the cool Humboldt Current from the south and the warm Panama Current from the northeast. These currents affect sea surface temperatures and modulate the stability of the overlying atmosphere.

The climate of the Galápagos Islands is characterized by two distinct seasons: a warm and rainy season from January to April, and a cool and 'dry' season from June to December (Fig. 1). The intermediate months bridge the warm and cool seasons. During the cool period, the ITCZ is positioned north of the Galápagos. Stronger trade winds push the cold water from the Humboldt Current to the north. Increased upwelling lowers the sea surface and air temperatures and leads to minimal convection over the ocean. As the cooler air is pushed towards the islands, it is trapped below the warmer air creating a temperature inversion and condensation where the two air masses meet (Trueman and d'Ouzouville, 2010). On the windward side of the islands, condensation usually occurs above 250 m altitude and leads to the formation of extensive stratus clouds (locally called 'garúa', Bush et al., 2010). The topography of the islands causes orographic lifting, adiabatic cooling, and further increase of the relative humidity. Thus, light rain, drizzle and orographic fog are characteristic of Santa Cruz island's highlands during the cool season (Alomia et al., 2024). Conversely, during the warm season, the ITCZ moves southward, trade winds weaken, and sea surface temperatures rise, resulting in the dissipation of the temperature inversion layer. This season is marked by strong convective air movements, resulting in short-lived but high-intensity rain in both the lower and upper regions of the island (Pryet et al., 2012; Trueman and D'Ozouville, 2010).

3. Materials and methods

3.1. Rainwater sampling and measurement along a climosequence on Santa Cruz Island

Santa Cruz Island features a pronounced precipitation gradient along its windward slope, ranging from dry lowlands to humid highlands, and an equatorial location that is ideal for exploring soil – water – vegetation

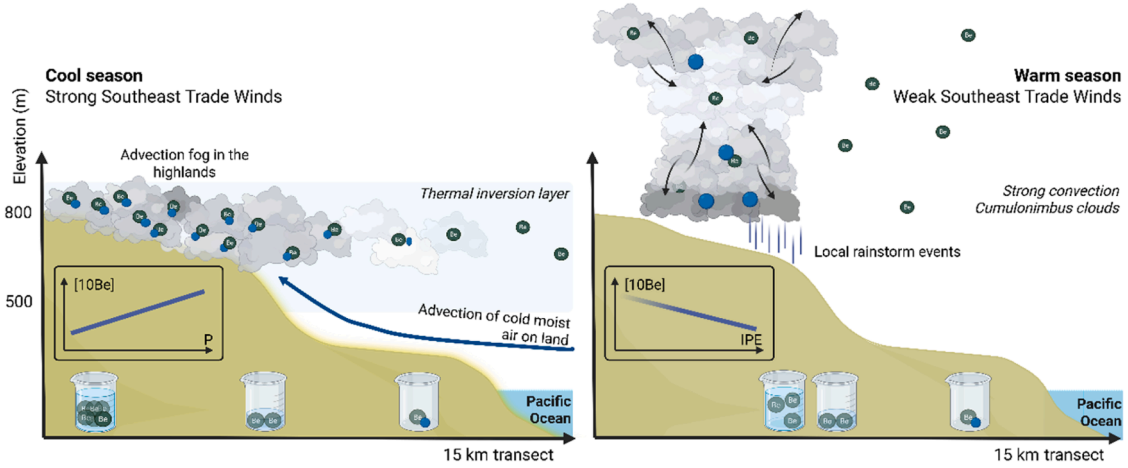

Fig. 1. Conceptual diagram illustrating the experimental setup with five sites covering a 10-fold precipitation gradient along the windward slopes of Santa Cruz Island that are exposed to southeast trade winds. This equatorial island is characterized by differences in rainfall type over the year. During the cool season, the trade winds bring the cool Humbold current towards the Galapagos, leading to the advection of cool air over the island and the development of a temperature inversion layer and stratus clouds. Above 400 m, advection fog resulting from orographic lifting is persistent, leading to a quasi-continuous precipitation of small fog and rain droplets (Pryet et al. 2012). During the warm season, the southeast trade winds weaken and intensive convection of warm air masses leads to the development of cumulonimbus clouds that are characterized by thorough vertical mixing and produce torrential rain with large rain drops. In the figure, the beakers represent sampling points where rain water was collected biweekly: the volume of water in the beaker is indicative of the precipitation rate, and the number of Be atoms of the $^{10}Be_m$ deposition. Created in BioRender. 2, S. (2025) https://BioRender.com/ijzcgnc.

interactions (e.g., Paque et al., 2024). This study on the variation in $^{10}Be_m$ depositional fluxes is an important methodological contribution to a larger thematic project that aims to use $^{10}Be_m$ for quantifying Earth surface dynamics. We installed five monitoring sites in 2021 along the northwest to southeast-oriented precipitation gradient on the windward side of the island (Fig. 2). The sites are located at five different elevations, ranging from 47 to 800 m a.s.l., capturing distinct precipitation regimes.

At each site a rainwater collector was installed (Fig. 2). Each collector was positioned two meters above the ground to minimize the influence of biota and local remobilization on water collection (Fig. S1). The collector was made of a PVC funnel covered with a 2 mm plastic mesh to prevent organic material accumulation. At the base of the funnel, a 20 µm nylon mesh was inserted to pre-filter the water. The funnel was directly connected to a 5 L amber glass bottle via a PVC hose, with all connections being tightly sealed to ensure rapid transfer of water from the collector to the bottle and reduce external

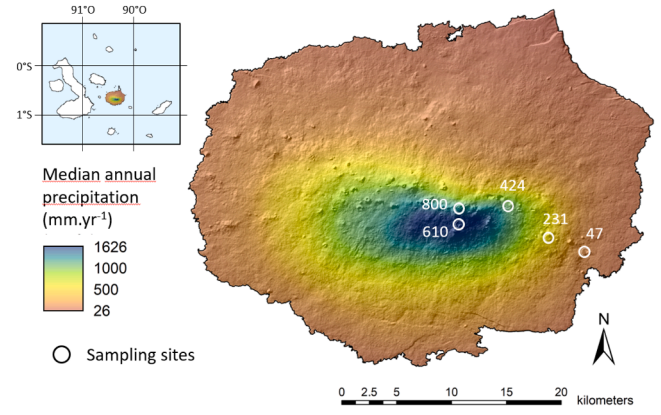

Fig. 2. Positions of the sampling sites. Upper left map indicates the location of Santa Cruz Island within the Galápagos Archipelago. The main map shows the location of the five sampling sites along a northwest to southeast-oriented climosequence. The sites are labelled with their respective elevations, and the text employs the prefix EC-SC. The background map shows the median annual precipitation (Alomia et al., 2022) overlaid on a 3D relief map. The reader is invited to read the web version of this article for interpretation of the colors.

contamination. The bottle was placed in a plastic bucket underground, and the area was covered by a wooden board to minimize temperature fluctuations. Before field deployment, all components - meshes, funnels, pipes, and bottles - underwent a thorough cleaning process, involving three cycles of acid cleaning with 0.5 M HNO_3, followed by extensive rinsing with ultra-pure water. The collectors were installed in early April 2021. During the first month, the bottles were emptied twice and the water discarded, allowing the system to reach equilibrium with respect to ion adsorption. Subsequently, the bottles were emptied at least every two weeks over one full hydrological year and the water retained for analysis (Table 1).

When studying the controls of precipitation on $^{10}Be_m$ deposition it is important to distinguish between wet and dry deposition. Both wet and dry deposition processes remove aerosols from the atmosphere, including $^{10}Be_m$. Dry deposition is predominantly associated with larger aerosol particles such as dust particles, typically greater than 50 µm, which settle due to gravity (Boucher, 2015). Their deposition depends on the aerodynamical resistance of the surface, which is related to the surface roughness and local winds (Heikkilä et al., 2013).

In contrast, wet deposition captures a broader range of particle sizes. While larger particles are scavenged by raindrops through processes like impaction and interception, smaller aerosols, up to < 0.1 µm, act as cloud condensation nuclei, facilitating their incorporation into precipitation (Boucher, 2015). Additionally, dust from locally eroded and remobilized soil can significantly increase $^{10}Be_m$ concentrations in rain samples (Graham et al. 2003; Lal, 2007).

To isolate wet deposition from local resuspended soil and long-range transported dust, the water was filtered using Sartorius 0.45 µm cellulose nitrate membranes directly after collection, to remove large dust particles, while retaining the dissolved and very fine particulate fractions that are most relevant to wet deposition dynamics. The collection bottles were emptied every two weeks. The water was combined with the previous collections during the sampling period and stored in a refrigerator at 4 °C until the end of the period. After filtration, the water was acidified to pH 2 by adding a few drops of HNO_3. We analyzed the $^{10}Be_m$ concentrations in the rain collected during the cool 'garua' season, the warm and rainy season, and the transition from the warm to cool season (Fig. 3). The collection dates of the 20 samples, 4 per site, and corresponding precipitation amounts are detailed in Table 1.

Table 1
Dates of rainwater collection, precipitation measurements from rain gauges during the sampling period, mean daily precipitation, percentage of intense precipitation events (IPE), and $^{10}Be_m$ concentrations in rainwater samples per period, with the 1σ uncertainty. Only for 10 % of the samples (indicated by *) was the $^{10}Be_m$ was estimated from a nearby site or consecutive period (see Supplementary Material, text S4).

	Collection dates	1	2	3	4
	Sites	01/05/2021 - 15/09/2021 Cool	15/09/2021 – 13/02/2022 Cool	13/02/2022 – 28/03/2022 Warm	28/03/2022 – 27/06/2022 Warm to Cool
Precipitation (mm)	EC-SC-47	49	45	143	27
Mean daily precipitation (mm/day)		0.4	0.3	3.3	0.3
IPE (%)		0.0	0.0	42	0.0
$[^{10}Be_m]_{rain}$ (x10^4 at/g_{H2O})		0.73*	0.73 ± 0.07	0.24 ± 0.01	0.68 ± 0.01
Precipitation (mm)	EC-SC-231	165	143	145	98
Mean daily precipitation (mm/day)		1.2	0.9	3.4	1.1
IPE (%)		0.0	0.0	19	0.0
$[^{10}Be_m]_{rain}$ (x10^4 at/g_{H2O})		1.06 ± 0.02	1.05 ± 0.02	0.73 ± 0.01	0.85 ± 0.01
Precipitation (mm)	EC-SC-424	263	195	239	176
Mean daily precipitation (mm/day)		1.9	1.3	5.6	1.9
IPE (%)		0.0	0.0	7.1	1.9
$[^{10}Be_m]_{rain}$ (x10^4 at/g_{H2O})		0.63 ± 0.01	1.13 ± 0.02	0.53 ± 0.01	0.73 ± 0.01
Precipitation (mm)	EC-SC-610	703	632	408	420
Mean daily precipitation (mm/day)		5.1	4.2	9.5	4.6
IPE (%)		4.7	0.8	15	7.2
$[^{10}Be_m]_{rain}$ (x10^4 at/g_{H2O})		0.98 ± 0.01	1.69 ± 0.03	0.42*	0.84 ± 0.01
Precipitation (mm)	EC-SC-800	704	631	688	463
Mean daily precipitation (mm/day)		5.1	4.2	16	5.1
IPE (%)		0.6	0.0	25	6.8
$[^{10}Be_m]_{rain}$ (x10^4 at/g_{H2O})		1.06 ± 0.03	1.66 ± 0.02	0.40 ± 0.02	0.90 ± 0.01

3.2. Precipitation measurements

To characterize the rainfall amount and intensity along the gradient, a tipping bucket pluviometer (Rainew Rain Gauge, Rainwise, resolution 0.20 mm) was installed at four sites (EC-SC-47, EC-SC-231, EC-SC-424, and EC-SC-610) and a complete meteorological station (METER ATMOS 41) at site EC-SC-800 (Fig. 2). Because of short periods of inactivity at certain stations, we generated a complete time series for each site using the methodology outlined by Longman et al. (2020).

To assess the influence of convective precipitation events that generate intense rainfall on $^{10}Be_m$ deposition, we quantified the contribution of intense precipitation to total annual precipitation for each study site and observational period. First, we defined an intense precipitation event as any instance where daily rainfall exceeds 15 mm. We then computed an intense precipitation index that corresponds to the proportion of annual precipitation that falls during intense precipitation events:

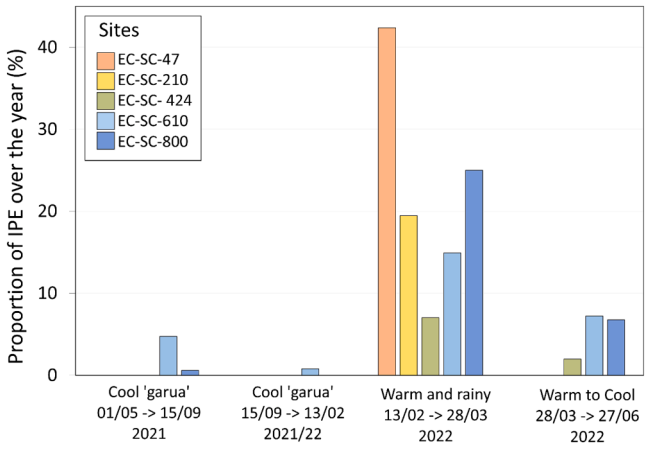

Fig. 3. Percentage of rain that falls during intense precipitation events (IPE) based on the 15 min. interval rainfall information recorded by the pluviometers at the sampling sites. For a detailed interpretation of the color schemes used in the visualizations, readers are encouraged to consult the online version of this article.

$$\text{IPE \%} = \left(\frac{\sum \text{Daily precipitation} > 15\ \text{mm}}{\text{Total annual precipitation}}\right) \times 100 \quad (1)$$

where IPE % is the percentage of annual precipitation that falls during intense precipitation events in the interval of interest. This calculation was performed separately for each period and site, allowing us to analyze temporal variations in intense precipitation across the sites. We use a 15 mm threshold across all sites to ensure comparability. Using thresholds of 10 mm/day, 20 mm/day, or 25 mm/day (Supplementary materials, Text. S2, Fig. S2) yield trends that are similar to 15 mm/day, indicating the robustness of our results to variations in the threshold for intense precipitation events.

3.3. Meteoric ^{10}Be in rainwater samples

At the end of each sampling period, we precipitated the Be from the rainwater samples so that a smaller sample volume could be transported to UCLouvain (Belgium) for further analysis. To have an external control on the recovery of the $^{10}Be_m$ during sample preparation, we added 100 µl of ^{9}Be carrier solution (146 µg/ml) to each sample. Subsequently, we added 10 mg of $FeCl_3$ per 1 L of rainwater, homogenized the mixture and allowed it to equilibrate for one hour. We precipitated $Fe(OH)_3$ and $Be(OH)_2$ by gradually adding $NH_3.H_2O$ until we achieved a pH of approximately 9 and orange floccules were visible (Fig. S1). The precipitates were allowed to settle for 12 h. We siphoned off the supernatant using a high-density polyethylene (HDPE) hose and took a 250 ml aliquot of the supernatant for quality control. We then redissolved the Be-precipitate by adding concentrated HNO_3, bringing the solution slowly to pH 2. Finally, we mixed and transferred the solution to 250 ml acid-cleaned Nalgene bottles for transportation.

3.4. $^{10}Be_m$ recovery, extraction, and measurement

At UCLouvain, the contents of the 250 ml Nalgene bottles were homogenized, transferred to 180 ml Teflon beakers, and evaporated. The residue was then dissolved in 15 ml of 3 M HNO_3 and a 0.5 ml aliquot was extracted. As we spiked the rainwater samples with ^{9}Be carrier solution, we used the total Be concentrations of the aliquots to obtain the recovery rates of Be. The average recovery rate was 78 %. Beryllium was extracted from the remaining solution through ion exchange chromatography, following the protocol outlined by von Blanckenburg et al. (1996).

Subsequently, $^{10}Be/^{9}Be$ ratios were measured on the MILEA

accelerator mass spectrometer (AMS) at ETH Zurich and normalized with in-house secondary ^{10}Be standards, S2007N and S2010N, with nominal values of $^{10}Be/^{9}Be = 28.1 \times 10^{-12}$ and 3.3×10^{-12}, respectively (Christl et al., 2013; Kubik and Christl, 2010). The $^{10}Be_m$ concentrations were adjusted based on the average of two procedural blanks that had a mean $^{10}Be/^{9}Be$ ratio of $3.69 \pm 1.15 \times 10^{-15}$. The estimated 1σ errors on $^{10}Be_m$ concentrations encompass the analytical uncertainty of the AMS measurements of the samples, as well as the weighing and blank error.

3.5. $^{10}Be_m$ concentrations and depositional fluxes

Our measurements provide novel constraints on the spatiotemporal variation in $^{10}Be_m$ concentrations in wet deposition across an equatorial climosequence (Table 1). We successfully determined ^{10}Be concentrations in 18 out of the 20 rainwater samples that were collected. However, 2 samples were lost during laboratory manipulations (period 1 at EC-SC-47 and period 3 at EC-SC-610). For these periods we estimated $^{10}Be_m$ concentrations using the measurements from an adjacent site or consecutive period (Supplementary Material, text S4).

In the results, we analyze the spatiotemporal variation in $^{10}Be_m$ concentrations for (1) all data points, (2) the warm and rainy period, and (3) the cool and transition periods. For the two latter, the mean $^{10}Be_m$ concentration per site is calculated as a precipitation-weighted average:

$$Mean(^{10}Be_m) = \sum_{t=1}^{i} [^{10}Be_m]_t \times P_t \Big/ \sum_{t=1}^{i} P_t \quad (2)$$

We computed $^{10}Be_m$ wet depositional fluxes (F_{10Be}, in at/cm^2/yr) at each site by multiplying the $^{10}Be_m$ concentrations ($[^{10}Be]_t$ in at/g) in rain water sampled during period, t, with the precipitation recorded by the pluviometers during that period (P_t, in cm/yr; Deng et al., 2020):

$$F_{^{10}Be_m} = \sum_{t=1}^{4} [^{10}Be_m]_t \times P_t \quad (3)$$

Analytical errors on the $^{10}Be_m$ concentrations were propagated to the $^{10}Be_m$ depositional fluxes. We assume that the calculated depositional fluxes account solely for wet deposition because the rain samples were filtered to exclude dry deposition and dust inputs.

To facilitate comparison with other databases of $^{10}Be_m$ depositional fluxes derived from rainwater measurements spanning different periods, we employed the normalization procedure outlined by Deng et al. (2020). This procedure involved two sequential steps to address changes in solar modulation and magnetic field intensity. First, the calculated fluxes were adjusted from the solar modulation potential during the collection period, which averaged 324 MeV to a standard solar modulation potential of 502 MeV, using the modelled relationship between the solar modulation parameter and global-averaged production rates (Masarik and Beer, 2009) for the contemporary magnetic field (Heikkilä et al., 2015). Second, $^{10}Be_m$ depositional fluxes were normalized to the average production rate over the Holocene epoch by multiplying by a factor of 1.23, representing the ratio between Holocene and modern production rates (Steinhilber et al., 2012). Further information about the normalization procedure is given in the Supplementary materials (Text S3). These normalization procedures ensure that our flux data are comparable with earlier and future work on $^{10}Be_m$ depositional fluxes.

4. Results

4.1. Convective events

The percentage of rain that falls during intense precipitation events, IPE, varied between the study sites and sampling periods. The lowest values are observed during the cool season that is characterized by fog and constant fine drizzle in the upper part of the island and by aridity in the lower part. During the cool season, the IPE ranges from 0 % at the drier sites (EC-SC-47, EC-SC-231, and EC-SC-424) to 4.74 % at the second wettest site (EC-SC-610). During the warm season, a considerable portion of the total rain falls during intense events, and this percentage varies with altitude: the lowest site (EC-SC-47) has the highest percentage of intense rain (42.4 %). This decreases with increasing altitude until the mid-altitudes (EC-SC-231 = 19.4 % and EC-SC-424 = 7.03 %), and then increases again with increasing altitude. The wettest site (EC-SC-800) has a quarter of the rain falling during intense precipitation events. This was primarily due to a single intense, localized thunderstorm (160 mm on the 26 of March 2022). As expected, the values are intermediate in the transition from the warm to cool season, with proportions varying between 0 % and 7.22 % (Fig. 3). Overall, the IPE is, on average, 35 times higher during the warm than the cool season, with the increase being largest at sites EC-SC-47 and EC-SC-800.

4.2. $^{10}Be_m$ concentrations

The $^{10}Be_m$ concentrations measured at the five sites vary between site and sampling period (Table 1). At site EC-SC-47, located in the arid part of the island, near the coast, $^{10}Be_m$ concentrations were highest during the cool season (7.27×10^3 at/g_{H20}) and lowest during the warm season (2.43×10^3 at/g_{H20}), with intermediate values during the transition from the warm to cool season (6.80×10^3 at/g_{H20}). Site EC-SC-210, located in the dry lowlands, had consistently higher $^{10}Be_m$ concentrations in the cool season (1.06×10^4 at/g_{H20}), and lower values during the warm season (7.31×10^3 at/g_{H20}) and transition period (8.52×10^3 at/g_{H20}). Site EC-SC-424, located in the intermediate zone of the precipitation gradient, showed slightly lower $^{10}Be_m$ concentrations during the warm season than the other periods (5.28×10^3 at/g_{H20} vs. 6.35×10^3 - 1.13×10^4 - 7.28×10^3 at/g_{H20}). At site EC-SC-610, in the humid highlands, the highest concentration was observed during the cool season (1.69×10^4 at/g_{H20}), and moderate values during the warm to cool transition (8.36×10^3 at/g_{H20}). Site EC-SC-800, the wettest site of the island, had the highest concentrations during the cool season (1.66×10^4 at/g_{H20}), lower values during the transition period (9.30×10^3 at/g_{H20}) and the lowest values during the warm rainy season (4.10×10^3 at/g_{H20}). Overall, $^{10}Be_m$ concentrations varied significantly between sites and seasons, with cool season samples generally showing higher $^{10}Be_m$ concentrations than warm season samples and the highlands exhibiting higher concentrations than the lowlands.

4.3. Relationship between $^{10}Be_m$ concentrations and precipitation

When analyzing depositional fluxes as a function of precipitation, an artificial self-correlation arises because the fluxes are the product of the $^{10}Be_m$ concentration and the precipitation rate. Therefore, we analyze how $^{10}Be_m$ concentrations, rather than $^{10}Be_m$ fluxes, vary with precipitation. The variation of $^{10}Be_m$ concentrations with precipitation at each site and sampling period is presented in Fig. 4. Measured $^{10}Be_m$ concentrations range from 0.24 to 1.69×10^4 at/g_{H20} across a range in collected precipitation of 27 to 704 mm, and average 0.85×10^4 at/g_{H20}. There is a substantial scatter in concentrations, especially at lower precipitation levels (below 200 mm), where $^{10}Be_m$ concentrations range from 0.23 (at site EC-SC-47) to 1.13×10^4 at/g_{H20} (at site EC-SC-424). As annual precipitation increases, the variability of $^{10}Be_m$ concentrations between sampling periods tends to increase. This is particularly evident for sites EC-SC-610 and EC-SC-800, where values range from 0.40 (at site EC-SC-800) to 1.69×10^4 at/g_{H20} (at site EC-SC-610). The observed spread in the $^{10}Be_m$ concentrations between the four sampling periods at all sites warrants examining whether $^{10}Be_m$ concentrations vary between orographic and convective precipitation events.

To isolate the signal of orographic precipitation, we focused on the period of advective rainfall during which there is a positive correlation between measured precipitation and the elevation of the sites ($r = 0.91$, p-value < 0.001, $n = 15$) and a low percentage of intense precipitation (Fig. 3). During this period of advective rainfall, the $^{10}Be_m$ concentrations showed a significant positive relation with the total recorded

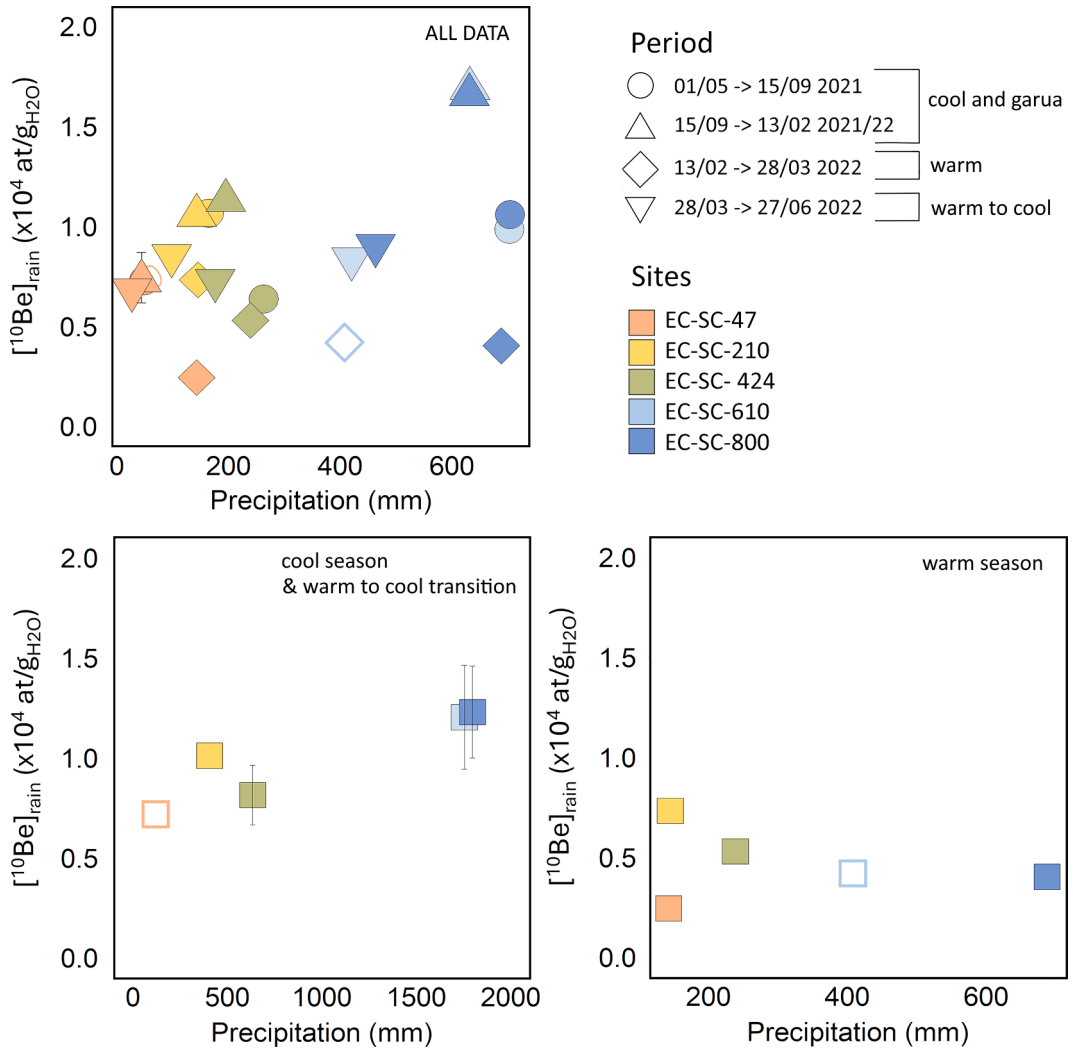

Fig. 4. Upper left: Measured $^{10}Be_m$ concentrations vs. precipitation for all sites and sampling periods. Error bars correspond to 1σ uncertainty; if not visible, they are smaller than the symbol. Lower left: Precipitation-weighted mean $^{10}Be_m$ concentrations for the cool and intermediate seasons. Error bars indicate the standard error of the mean. Lower right: Precipitation-weighted mean $^{10}Be_m$ concentrations for the warm rainy season. The 1σ uncertainty is smaller than the symbol. Empty squares indicate data points that include one sample with an estimated concentration. For color interpretation, refer to the online version of the article.

precipitation (Fig. 4; Spearman correlation coefficient, $r = 0.82$, $p < 0.05$, $n = 5$) although local variation in the $^{10}Be_m$ concentrations remained considerable. During the period of convective rainfall, the $^{10}Be_m$ concentrations decreased with increasing precipitation amounts, with the exception of the driest site (EC-SC-47) where the lowest concentration was registered (0.23×10^4 at/g_{H20}).

4.4. $^{10}Be_m$ concentrations during convective events

The $^{10}Be_m$ concentrations decrease markedly with an increasing percentage of intense precipitation (Fig. 5). Concentrations at the wettest site (EC-SC-800) fall by a factor of four (1.66×10^4 to 0.40×10^4 at/g_{H20}) as the percentage of intense precipitation increases from 0 % to 25 % (Tab.1). Similarly, $^{10}Be_m$ concentrations measured at the driest site fall by a factor of three (0.73×10^4 to 0.24×10^4 at/g_{H20}) from the cool to the warm, rainy period. This behavior aligns with the observation that the lowest $^{10}Be_m$ concentrations at each site were consistently measured during the period with the highest convective activity and the most intense precipitation events.

4.5. Annual meteoric ^{10}Be depositional fluxes

The results reveal an increase in annual depositional fluxes with precipitation, ranging from 1.34×10^5 at/cm^2/yr at the driest study site (EC-SC-47) to 27.6×10^5 at/cm^2/yr at the wettest site (EC-SC-800). There is a significant positive correlation between annual depositional fluxes and precipitation across the five study sites (Spearman correlation test, $r = 0.99$, $p < 0.001$, $n = 5$; Fig. 6a). However, this is partly due to the self-correlation between precipitation and the $^{10}Be_m$ flux.

We compare the measured annual fluxes after the normalization outlined in section 3.5 with model estimates of $^{10}Be_m$ deposition derived from global circulation modeling by Heikkilä and von Blanckenburg (2015) and the latitude-rainfall empirical model proposed by Graly et al. (2011) in Fig. 6a. The global circulation model operates at a spatial resolution of 2.8° x 2.8°, and as a result, Santa Cruz Island falls entirely within a single grid cell. Based on this model, the estimated average $^{10}Be_m$ flux for the island is 1.95×10^6 atoms/cm^2/yr. Using this average flux would overestimate the measured fluxes in the lower part of the island and underestimate them in the humid highlands. Conversely, the Graly model assumes a linear relationship between precipitation and $^{10}Be_m$ flux, with a constant $^{10}Be_m$ concentration in precipitation. Meteoric ^{10}Be fluxes on Santa Cruz Island also exhibit a nearly linear

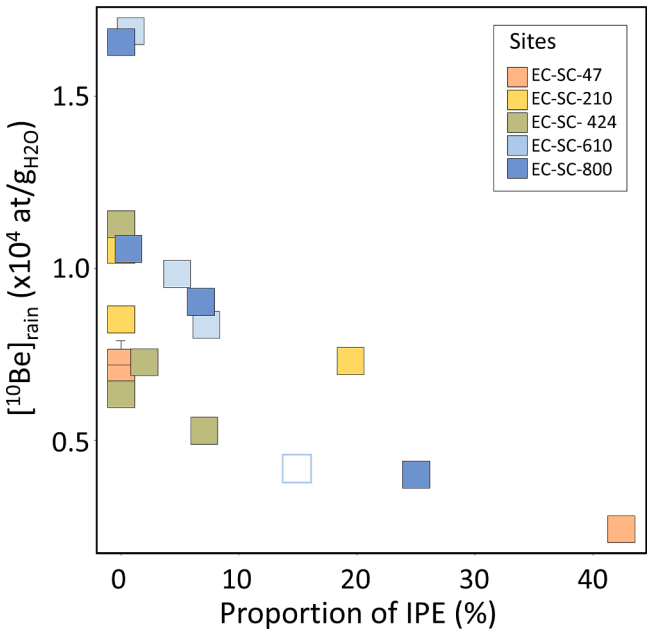

Fig. 5. Measured $^{10}Be_m$ concentrations vs. percentage of intense precipitation events (IPE) for each period and sampling site along the climosequence. The 1σ uncertainty is generally smaller than the symbol. Empty squares represent samples with estimated concentrations. For a detailed interpretation of the color schemes used in the visualizations, readers are encouraged to consult the online version of this article.

increase with precipitation. Thus, they are relatively well represented by the Graly model, although this model slightly overestimates fluxes at the low precipitation sites and underestimates them at the high precipitation sites. The root mean squared error (RMSE) between observed and modeled fluxes is approximately 4.09 × 10^5 at/cm^2/yr.

5. Discussion

5.1. Additive effect of orographic precipitation on $^{10}Be_m$ deposition

Our measurements along a climosequence, where average annual precipitation increases tenfold between the dry lowlands and the humid highlands, support that orographic precipitation enhances $^{10}Be_m$ deposition (Fig. 4). There is a positive correlation between mean annual $^{10}Be_m$ concentrations and annual precipitation (Spearman correlation coefficient, $r = 0.82$, $p < 0.05$, $n = 5$; Fig. 6b). Notably, this correlation is strongly dependent on the elevated cool-season $^{10}Be_m$ concentrations measured at sites EC-SC-610 and EC-SC-800. For example, during the cool and intermediate seasons precipitation is 15 times higher at the wettest site (EC-SC-800) than the driest site (EC-SC-47) and $^{10}Be_m$ concentrations are 1.7 times higher (Fig. 4).

The unique climate of the Galápagos Islands may explain the higher cool season $^{10}Be_m$ concentrations in the humid highlands. During the cool season, the sea surface temperature around the Galápagos decreases by 3 to 4 °C and cools the air over the ocean (Trueman and d'Ouzouville, 2010). The advection of cooler air from the Pacific Ocean on the windward side of the islands creates a temperature inversion layer, where cool air is trapped under warmer moist air, creating extensive stratus clouds. During this season, the lowlands (EC-SC-47) receive little moisture input: the daily relative air humidity rarely exceeds 90 % and condensation generally occurs above approximately 250 m altitude (Trueman and d'Ozouville, 2010).

The thermal inversion prevents vertical atmospheric mixing, and the cool oceanic air masses enriched in $^{10}Be_m$ are orographically lifted along the windward slopes up to the summit of the island. Stable isotope measurements in precipitation ($\delta^{18}O_p$ and δD_p) also showed consistent change with elevation (Martin et al., 2018), pointing to progressive condensation and precipitation during orographic lifting of the air masses. At elevations above 600 m, the relative humidity in the rising air is close to or at 100 % and condensation occurs, creating fog that contains microscopic water droplets that form on aerosol particles. These fog droplets are known to be effective in scavenging aerosol particles, such as $^{10}Be_m$, from the moist air and incorporating them in the fog water (Sonwani, 2025). This mechanism can explain why the sustained but light rain and drizzle that falls during the 'garua' season in the highlands (Alomia et al., 2024; Pryet et al., 2012; Trueman and d'Ozouville, 2010) contains particularly high $^{10}Be_m$ concentrations when the inversion layer is well-developed (Fig. 1). During this period, the $^{10}Be_m$ concentrations in rainfall are ca. 70 % higher in the highlands than in the lowlands, while the highlands receive fifteen times more precipitation (Fig. 4).

5.2. Dilution effect of convective precipitation on $^{10}Be_m$ deposition

Dilution can be facilitated by two mechanisms: the rapid removal of $^{10}Be_m$ from air masses through intense precipitation, and the entrainment of $^{10}Be_m$-depleted moisture from lower atmospheric levels during intense convective events (Deng et al., 2020; Willenbring and von Blanckenburg, 2010). Convective processes involve the rapid vertical ascent of warm, moist air from near the Earth's surface to higher altitudes, facilitating the transport of moisture and the influx of $^{10}Be_m$-depleted air masses from the marine boundary layer into the rain-forming regions of the atmosphere (Jordan et al., 2003; Fig. 1). The decline in $^{10}Be_m$ concentration with increasing proportion of intense precipitation events observed at the study sites (Fig. 5) demonstrates that the dilution effect influences $^{10}Be_m$ fluxes in the Galápagos. The measured $^{10}Be_m$ concentrations are consistently lower during the warm season, likely because of the predominance of the dilution effect during convective rainstorms that generate intense precipitation (Fig. 4). Concentrations measured in samples collected during the cool season were 1.45 to 3.34 times higher than those during the warm season. The most significant differences in concentrations are observed at sites EC-SC-47, EC-SC-610, and EC-SC-800, which experienced the greatest proportion of intense precipitation (Fig. 3).

5.3. Impact of competing additive and dilution effects on $^{10}Be_m$ fluxes

Our results suggest that the additive and dilution effects are in competition along the Santa Cruz climosequence but that on the annual scale the additive effect dominates. This can be seen when plotting the mean annual concentration of $^{10}Be_m$ in rainwater against the precipitation rate (Fig. 6B) or the inverse of precipitation rate (1/P) (Fig. 7). The negative slope in Fig. 7 ($S = -1.55 \times 10^5$) suggests a super-additive effect, with $^{10}Be_m$ concentrations increasing as precipitation increases. However, dilution during the warm, rainy season acts to partially mitigate the overall super-additive trend, as shown by $^{10}Be_m$ concentrations decreasing markedly with an increasing percentage of intense precipitation (Fig. 5).

Our findings differ from those reported on other tropical islands, where ^{7}Be concentrations - which are expected to behave similarly to $^{10}Be_m$ - typically increase with 1/P, indicating that the dilution effect is dominant. For example, on islands such as Mauna Loa (Hawaii), Pago (Samoa), and Easter Island, ^{7}Be fluxes, and by extension $^{10}Be_m$ fluxes, are diluted as precipitation rates increase (Feely et al., 1989 in Willenbring and von Blanckenburg, 2010). Our results from Santa Cruz Island reveal a more complex interaction between precipitation and $^{10}Be_m$, in which the significance of dilution depends on the proportion of precipitation falling in intense rainfall events, rather than the total precipitation, and in which seasonal atmospheric mixing patterns affect $^{10}Be_m$ wet deposition rates.

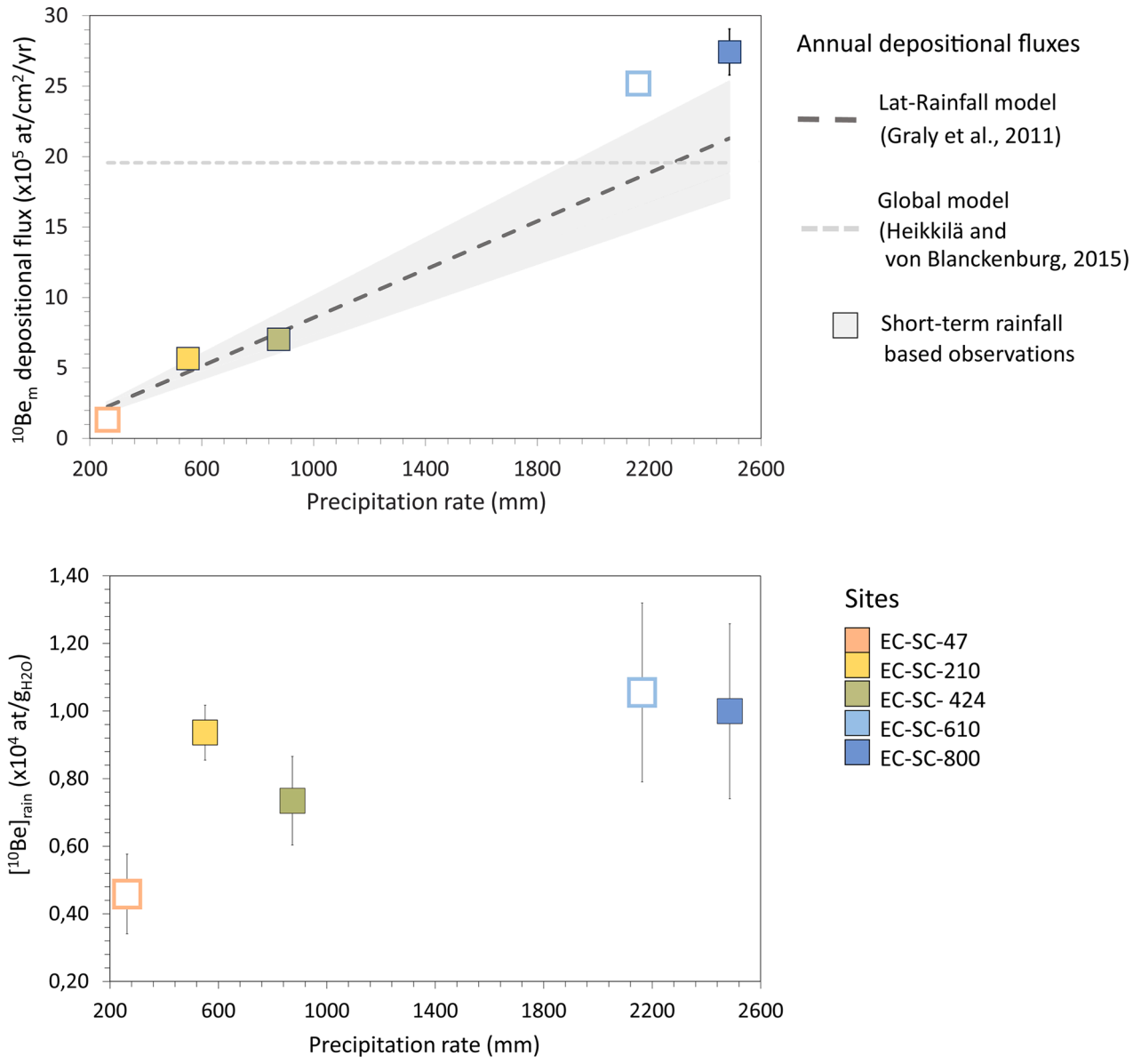

Fig. 6. (Top) The $^{10}Be_m$ depositional flux along the climosequence against cumulative annual precipitation. Data points show normalized annual fluxes derived from $^{10}Be_m$ measurements in rainfall. The 1σ uncertainties are generally smaller than the data points. These are compared with normalized flux estimates from the latitude-rainfall empirical model proposed by Graly et al. (2011) and global modeling by Heikkilä and von Blanckenburg (2015). The grey shaded area delineates a 20 % uncertainty on the Graly model's flux estimates. (Bottom) Precipitation-weighted mean $^{10}Be_m$ concentrations for the entire sampling year. Error bars indicate the standard error of the mean. Empty squares represent flux estimates where the concentration during one (out of 4) sampling periods was estimated by interpolation (Supplementary Materials, Text S4). For a detailed interpretation of the color schemes used in the visualizations, readers are encouraged to consult the online version of this article.

5.4. *Long-term delivery of $^{10}Be_m$ to the earth surface*

It is important to note that our study, which encompasses one year of measurements, does not capture inter-annual variability. Records of $^{10}Be_m$ in ice and ocean sediment cores indicate variations in $^{10}Be_m$ fluxes exceeding 50 % over timescales of 10^4 years (Finkel and Nishiizumi, 1997). These findings suggest that while short-term fluxes can be determined with relative accuracy, long-term fluxes may differ, in part due to changes in climatic factors. For example, convective activity in the Galápagos is influenced by large-scale climate phenomena, such as the El Niño-Southern Oscillation (ENSO). During El Niño events, the warmer sea surface temperatures in the equatorial Pacific enhance convective activity and increase precipitation (Trueman and d'Ozouville, 2010). During weak to moderate El Niño events, the convective processes are like those observed during the measurement period (Martin et al., 2018). In contrast, during very strong El Niño events, sea surface temperatures exceed a critical threshold of 28 °C, triggering large-scale convective processes. These events bring in air masses from higher atmospheric layers and transport them over longer distances, resulting in lower $\delta^{18}O$ values, as observed during the 1997/1998 El Niño (Martin et al., 2018). This intensified convective activity during strong El Niño events likely strengthens the dilution effect on $^{10}Be_m$ concentrations in precipitation during the warm, rainy season. In contrast, La Niña conditions, observed during the year of this study and characterized by cooler sea surface temperatures, typically reduce convection, leading to drier conditions and a diminished impact of the dilution effect on $^{10}Be_m$ depositional fluxes. Consequently, it is crucial to obtain long-term records to better understand inter-annual variations in $^{10}Be_m$ fluxes.

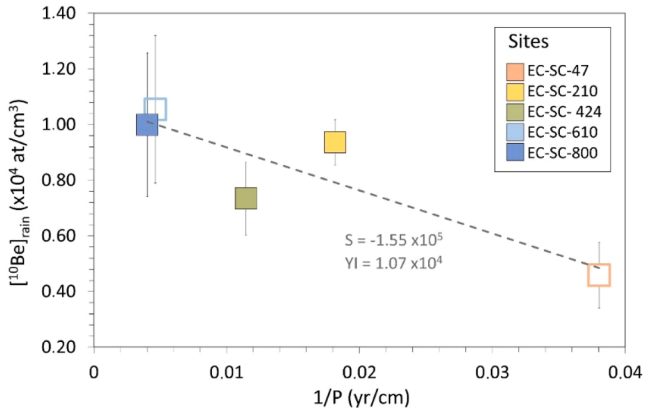

Fig. 7. Mean annual concentration of $^{10}Be_m$ plotted against the inverse of annual precipitation (1/P) for each site along the climosequence. Error bars indicate the standard error of the mean concentration. The slope (S) and y-intercept (YI) are indicated. For a detailed interpretation of the color schemes used in the visualizations, readers are encouraged to consult the online version of this article.

6. Conclusions

We reported measurements of $^{10}Be_m$ concentrations in rainwater and rain-gauge data from a climosequence on the windward slope of Santa Cruz Island, Galápagos that span one meteorological year. We sampled four distinct periods, including two in the cool season, one in the warm and rainy season, and a transitional period. By filtering the rainwater to isolate wet deposition, we analyzed the impact of precipitation type on $^{10}Be_m$ concentrations in rainwater and, hence, wet-depositional fluxes. Our findings reveal a rise in $^{10}Be_m$ deposition rates with precipitation that exceeds a linear increase, indicating a super-additive effect of precipitation on $^{10}Be_m$ deposition. We attribute this to the presence of a thermal inversion layer on Santa Cruz Island during the cool season, which limits vertical atmospheric mixing. Furthermore, we observed a clear decline in $^{10}Be_m$ concentrations with increased convective precipitation during the warm and rainy season. This suggests a dilution effect on atmospheric $^{10}Be_m$ deposition during intense precipitation events when vertical atmospheric mixing is enhanced. However, on an annual scale, the additive effect outweighs the dilution effect. These results underscore the multifaceted interplay between precipitation dynamics and $^{10}Be_m$ deposition at equatorial latitudes.

CRediT authorship contribution statement

Rose PAQUE: Writing – original draft, Visualization, Methodology, Investigation, Formal analysis, Data curation, Conceptualization. **Angus MOORE:** Writing – review & editing, Validation. **Jean L. DIXON:** Supervision, Methodology, Conceptualization. **Marcus CHRISTL:** Formal analysis. **Yessenia MONTES:** Data curation. **Veerle VANACKER:** Writing – review & editing, Visualization, Supervision, Resources, Project administration, Methodology, Funding acquisition, Conceptualization.

Declaration of competing interest

We declare that there are no conflicts of interest or financial or personal relationships that could inappropriately influence or bias the content of this work.

We confirm that all data and interpretations in this manuscript are entirely independent of the funding sources.

Acknowledgements

This study was conducted under research permits no. PC-01–21 and PC-45–22 granted by the Galápagos National Park. The team of the Central University of Ecuador (UCE), in particular Dr. Ilia Alomía Herrera from FIGEMPA and biologist Xavier Salazar from the Galapagos campus of UCE greatly facilitated our research through their support during field campaigns and research administration. We extend our gratitude to the team at Galápagos National Park, particularly Mr. Steve Bayas and Mrs. Evelyn Vera, and the Ecological Reserve "Cerro Mesa" for their continuous support. We also thank the park rangers and field assistant, Mr. Miguel Moncayo, for their technical assistance in the field. Laboratory work in the cosmogenic radionuclide laboratory at ELI-UCLouvain was facilitated by Dylan Vellut. Laurence Monin and Elodie Devos performed the ICP measurements at the analytical platform MOCA. This research was supported by the Fonds Spéciaux de la Recherche of UCLouvain (FSR2019 ARH/LJB/01133710) and the Fonds de la Recherche Scientifique – FNRS under PDR Grant n° T.0211.2022 (SoilScapeBasalt), and the Institutional Support Program to the Central University of Ecuador, supported by the Académie de Recherche et Education Supérieur de la Fédération Wallonie-Bruxelles (ARES CCD) and funded through the Belgian development cooperation. We thank the two anonymous reviewers for their insightful and constructive comments that helped us to clarify the concepts related to meteoric beryllium deposition processes and patterns.

Supplementary materials

Supplementary material associated with this article can be found, in the online version, at doi:10.1016/j.epsl.2025.119759.

Data availability

Beryllium in rainwater: original data is publicly available on zenodo via doi:10.5281/zenodo.14228934.

References

Alomía Herrera, I., Paque, R., Maertens, M., Vanacker, V., 2022. History of land cover change on Santa Cruz Island. Galapagos. Land 11 (7), 1017. https://doi.org/10.3390/land11071017.

Alomia Herrera, I., Molina, A., Montes, Y., Dixon, J.L., Vanacker, V., 2024. Evaluation of nature-based climate solutions for agricultural landscapes in the Galápagos Islands. Glob Planet Change 243, 104598. https://doi.org/10.1016/j.gloplacha.2024.104598.

Bacon, A.R., Richter, D.B., Bierman, P.R., Rood, D.H., 2012. Coupling meteoric ^{10}Be with pedogenic losses of 9Be to improve soil residence time estimates on an ancient North American interfluve. Geology 40, 847–850. https://doi.org/10.1130/G33449.1.

Beer, J., Blinov, A., Bonani, G., Finkel, R.C., Hofmann, H.J., Lehmann, B., Oeschger, H., Sigg, A., Schwander, J., Staffelbach, T., Stauffer, B., Suter, M., Wötfli, W., 1990. Use of ^{10}Be in polar ice to trace the 11-year cycle of solar activity. Nature 347, 164–166. https://doi.org/10.1038/347164a0.

von Blanckenburg, F., Belshaw, N.S., O'nions, R.K., 1996. Separation of ^{9}Be and cosmogenic ^{10}Be from environmental materials and SIMS isotope dilution analysis. Chem. Geol. 129, 93–99. https://doi.org/10.1016/0009-2541(95)00157-3.

Brown, L., Gary, J.S., Jeffrey, K., Roy, M., 1989. Atmospheric deposition of ^{7}Be and ^{10}Be. Chem. Geol. 53, 303–315. https://doi.org/10.1016/0016-7037(89)90280-9.

Brown, L., Pavich, M.J., Hickman, R.E., Klein, J., Middleton, R., 1988. Erosion of the eastern United States observed with ^{10}Be. Earth Surf. Process. Landforms 13, 441–457. https://doi.org/10.1002/esp.3290130509.

Boucher, O., 2015. Atmospheric aerosols. Atmospheric Aerosols. Springer, Dordrecht. https://doi.org/10.1007/978-94-017-9649-1.

Bush, M.B., Colinvaux, P.A., Steinitz-Kannan, M., Overpeck, J.T., Sachs, J., Cole, J., Collins, A., Conroy, J., Restrepo, A., Zhang, Z., 2010. Forty years of paleoecology in the Galápagos. Galapagos Res. 67, 55–61.

Christl, M., Vockenhuber, C., Kubik, P.W., Wacker, L., Lachner, J., Alfimov, V., Synal, H. A., 2013. The ETH Zurich AMS facilities: performance parameters and reference materials. Nucl. Instrum. Methods Phys. Res. B 294, 29–38. https://doi.org/10.1016/j.nimb.2012.03.004.

Deng, K., Wittmann, H., von Blanckenburg, F., 2020. The depositional flux of meteoric cosmogenic ^{10}Be from modeling and observation. Earth Planet. Sci. Lett. 550, 116530. https://doi.org/10.1016/j.epsl.2020.116530.

Dixon, J.L., Chadwick, O.A., Pavich, M.J., 2018. Climatically controlled delivery and retention of meteoric ^{10}Be in soils. Geology 46, 899–902. https://doi.org/10.1130/G45176.1.

Egli, M., Brandová, D., Böhlert, R., Favilli, F., Kubik, P.W., 2010. ^{10}Be inventories in alpine soils and their potential for dating land surfaces. Geomorphology 119, 62–73. https://doi.org/10.1016/j.geomorph.2010.02.019.

Feely, H.W., Larsen, R.J., Sanderson, C.G., 1989. Factors that cause seasonal variations in beryllium-7 concentrations in surface air. J. Environ. Radioact. 9, 223–249. https://doi.org/10.1016/0265-931X(89)90046-5.

Field, C., Schmidt, G., Koch, D., Salyk, C., 2006. Modeling production and climate-related impacts on 10Be concentration in ice cores. J. Geophys. Res. 111, D15107. https://doi.org/10.1029/2005JD00640.

Finkel, R.C., Nishiizumi, K., 1997. Beryllium 10 concentrations in the Greenland Ice Sheet Project 2 ice core from 3 to 40 ka. J. Geophys. Res. Oceans 102, 26699–26706. https://doi.org/10.1029/97JC01282.

Graham, I., Ditchburn, R., Barry, B., 2003. Atmospheric deposition of ^{7}Be and ^{10}Be in New Zealand rain (1996–1998). Chem. Geol. 201, 307–321. https://doi.org/10.1016/S0016-7037(02)01092-X.

Graly, J.A., Reusser, L.J., Bierman, P.R., 2011. Short and long-term delivery rates of meteoric ^{10}Be to terrestrial soils. Earth Planet. Sci. Lett. 302, 329–336. https://doi.org/10.1016/j.epsl.2010.12.020.

Heikkilä, U., Beer, J., Abreu, J., Steinhilber, F., 2013. On the atmospheric transport and deposition of the cosmogenic radionuclides (^{10}Be): a review. Space Sci. Rev. 176, 321–332. https://doi.org/10.1007/s11214-011-9838-0.

Heikkilä, U., Beer, J., Alfimov, V., 2008. Beryllium-10 and beryllium-7 in precipitation in Dübendorf (440 m) and at Jungfraujoch (3580 m), Switzerland (1998–2005). J. Geophys. Res. Atmos. 113, D11104. https://doi.org/10.1029/2007JD009160.

Heikkilä, U., von Blanckenburg, F., 2015. The global distribution of Holocene meteoric 10Be fluxes from atmospheric models. Distribution maps for terrestrial Earth surface applications, GFZ Data Services, GFZ Potsdam, Germany. doi:10.5880/GFZ.2.2.2015.001.

Heikkilä, U., Beer, J., Feichter, J., 2009. Meridional transport and deposition of atmospheric ^{10}Be. Atmos. Chem. Phys. 9, 515–527. https://doi.org/10.5194/acp-9-515-2009.

Jordan, C.E., Dibb, J.E., Finkel, R.C., 2003. ^{10}Be/^{7}Be tracer of atmospheric transport and stratosphere-troposphere exchange. J. Geophys. Res. Atmos. 108, 4234. https://doi.org/10.1029/2002JD002395.

Jungers, M.C., Bierman, P.R., Matmon, A., Nichols, K., Larsen, J., Finkel, R., 2009. Tracing hillslope sediment production and transport with in situ and meteoric ^{10}Be. J. Geophys. Res. Earth Surf. 114, F04019. https://doi.org/10.1029/2008JF001086.

Krone, L., Wittmann, H., von Blanckenburg, F., 2024. Precipitation control on weathering intensity and depositional flux of meteoric 10Be revealed from soil profiles along a climate gradient (Chile). Geophys. Res. Lett. 51, e2024GL108815. https://doi.org/10.1029/2024GL108825.

Kubik, P.W., Christl, M., 2010. ^{10}Be and ^{26}Al measurements at the Zurich 6 MV tandem AMS facility. Nucl. Instrum. Methods Phys. Res. B 268, 880–883. https://doi.org/10.1016/j.nimb.2009.10.054.

Lal, D., Peters, B., 1967. Cosmic ray produced radioactivity on the Earth. Handbuch Der Physik. Springer-Verlag, New York, pp. 551–612.

Lal, D., 2007. Recycling of cosmogenic nuclides after their removal from the atmosphere: special case of appreciable transport of ^{10}Be to polar regions by aeolian dust. Earth Planet. Sci. Lett. 264, 177–187. https://doi.org/10.1016/j.epsl.2007.09.030.

Lebatard, A.E., Bourlès, D.L., Braucher, R., Arnold, M., Duringer, P., Jolivet, M., et al., 2010. Application of the authigenic ^{10}Be/^{9}Be dating method to continental sediments: reconstruction of the Mio-pleistocene sedimentary sequence in the early hominid fossiliferous areas of the northern Chad Basin. Earth Planet. Sci. Lett. 297, 57–70. https://doi.org/10.1016/j.epsl.2010.06.003.

Longman, R.J., Newman, A.J., Giambelluca, T.W., Lucas, M., 2020. Characterizing the uncertainty and assessing the value of gap-filled daily rainfall data in Hawaii. J. Appl. Meteorol. Climatol. 59, 1261–1276. https://doi.org/10.1175/JAMC-D-20-0007.1.

Masarik, J., Beer, J., 2009. An updated simulation of particle fluxes and cosmogenic nuclide production in the Earth's atmosphere. J. Geophys. Res. Atmos. 114, D11103. https://doi.org/10.1029/1998JD200091.

Martin, N.J., Conroy, J.L., Noone, D., Cobb, K.M., Konecky, B.L., Rea, S., 2018. Seasonal and ENSO influences on the stable isotopic composition of Galápagos precipitation. J. Geophys. Res. Atmos. 123, 261–275. https://doi.org/10.1002/2017JD027380.

McHargue, L.R., Damon, P.E., 1991. The global beryllium 10 cycle. Rev. Geophys. 29, 141–158. https://doi.org/10.1029/91RG00072.

Monaghan, M.C., McKean, J., Dietrich, W., Klein, J., 1992. ^{10}Be chronometry of bedrock-to-soil conversion rates. Earth Planet. Sci. Lett. 111, 483–492. https://doi.org/10.1016/0012-821X(92)90198-5.

Paque, R., Alomia Herrera, I., Dixon, J.L., Molina, A., Zehetner, F., Vanacker, V., 2024. Constraining the effect of climate and rock porosity on weathering extent in the volcanic island of Santa Cruz (Galápagos, Ecuador). J. Geophys. Res.: Earth Surf. 129, e2024JF007651. https://doi.org/10.1029/2024JF007651.

Pavich, M.J., Brown, L., Valette-Silver, J.N., Klein, J., Middleton, R., 1985. ^{10}Be analysis of a quaternary weathering profile in the Virginia Piedmont. Geology 13, 39–41. https://doi.org/10.1130/0091-7613(1985)13<39:BAOAQW>2.0.CO;2.

Portenga, E.W., Bierman, P.R., Trodick, C.D., Greene, S.E., DeJong, B.D., Rood, D.H., Pavich, M.J., 2019. Erosion rates and sediment flux within the Potomac River basin quantified over millennial timescales using beryllium isotopes. GSA Bull 131, 1295–1311. https://doi.org/10.1130/B31840.1.

Pryet, A., Dominguez, C., Fuente Tomai, P., Chaumont, C., Villacís, M., Violette, S., 2012. Quantification of cloud water interception along the windward slope of Santa Cruz Island, Galápagos (Ecuador). Geophys. Res. Lett. 39, L05402. https://doi.org/10.1016/j.agrformet.2012.03.018.

Schoonejans, J., Vanacker, V., Opfergelt, S., Christl, M., 2017. Long-term soil erosion derived from in-situ ^{10}Be and inventories of meteoric ^{10}Be in deeply weathered soils in southern Brazil. Chem. Geol. 466, 380–388. https://doi.org/10.1016/j.chemgeo.2017.06.025.

Sonwani, S., 2025. Perspectives on fog chemistry: characteristics, variability, and its scavenging efficiency. In: Saxena, P., Gupta, A.K., Sorí, R. (Eds.), Fog: Formation, Chemistry, Dynamics, Impact and Dissipation. Springer Nature Singapore Pte Ltd, pp. 41–58.

Steinhilber, F., Abreu, J.A., Beer, J., Brunner, I., Christl, M., Fischer, H., et al., 2012. 9400 years of cosmic radiation and solar activity from ice cores and tree rings. Proc. Natl. Acad. Sci. U.S.A. 109, 5967–5971. https://doi.org/10.1073/pnas.1118965109.

Trueman, M., D'Ozouville, N., 2010. Characterizing the Galápagos terrestrial climate in the face of global climate change. Galápagos Res 67, 26–37.

Wang, C., Fiedler, P.C., 2006. ENSO variability and the eastern tropical Pacific: a review. Prog. Oceanogr. 69, 239–266. https://doi.org/10.1016/j.pocean.2006.03.004.

West, N., Kirby, E., Bierman, P., Slingerland, R., Ma, L., Rood, D., Brantley, S., 2013. Regolith production and transport at the Susquehanna Shale Hills Critical Zone Observatory, part 2: insights from meteoric ^{10}Be. J. Geophys. Res. Earth Surf. 118, 1877–1896. https://doi.org/10.1002/jgrf.20121.

Willenbring, J.K., von Blanckenburg, F., 2010. Meteoric cosmogenic beryllium-10 adsorbed to river sediment and soil: applications for earth-surface dynamics. Earth Sci. Rev. 98, 105–122. https://doi.org/10.1016/j.earscirev.2009.10.008.

Wittmann, H., von Blanckenburg, F., Dannhaus, N., Bouchez, J., Gaillardet, J., Guyot, J. L., et al., 2015. A test of the cosmogenic ^{10}Be(meteoric)/^{9}Be proxy for simultaneously determining basin-wide erosion rates, denudation rates, and the degree of weathering in the Amazon basin. J. Geophys. Res. Earth Surf. 120, 2498–2528. https://doi.org/10.1002/2015JF003581.